Fe Nitride Formation in Fe–Si Alloys: Crystallographic and Thermodynamic Aspects

STEFAN KANTE and ANDREAS LEINEWEBER

A Fe–3wt pctSi alloy was gas nitrided to study the effect of Si on the Fe nitride formation. Both ε-Fe$_3$N$_{1+x}$ and γ'-Fe$_4$N were observed at nitriding conditions only allowing to form single-phase γ' layers in pure α-Fe. During short nitriding times, ε and γ' simultaneously grow in contact with Si-supersaturated α-Fe(Si). Both nitrides almost invariably exhibit crystallographic orientation relationships with α-Fe, which are indicative of a partially displacive transformation of α-Fe being involved in the initial formation of ε and γ'. Due to Si constraining the Fe nitride growth, such transformation mechanism becomes highly important to the nitride layer formation, causing α-Fe-grain-dependent variations in the nitride layer morphology and thickness, as well as microstructure refinement within the nitride layer. After prolonged nitriding, α-Fe is depleted in Si due the pronounced precipitation of Si-rich nitride in α-Fe. The growth mode of the compound layer changes, now advancing by conventional planar-type growth. During nitriding times of 1 to 48 hours, ε exists in contact with the NH$_3$/H$_2$-containing nitriding atmosphere at a nitriding potential of 1 atm$^{-1/2}$ and 540 °C, only allowing for the formation of γ' in pure Fe, indicating that Si affects the thermodynamic stability ranges of ε and γ'.

I. INTRODUCTION

THE design of Fe-base alloys often requires additions of Si. Ferritic and pearlitic cast irons contain up to 3 wt pct Si to promote the formation of graphite during solidification.[1] Martensitic and bainitic ultra-high strength and tool steels are alloyed with Si to inhibit or modify the precipitation of carbides.[2–4] Nitriding is applied to improve the tribological properties and corrosion resistance of the aforementioned steels[5–9] and cast irons.[10–13] The improvement results from the formation of a surface layer composed of Fe nitrides, γ'-Fe$_4$N and ε-Fe$_3$N$_{1+x}$ (Table I), the so-called *compound layer*, and the precipitation of alloying element nitrides in the N-enriched *diffusion zone* underneath the compound layer. Understanding the role of Si in the nitride formation is required to tailor nitriding processes of the above steels and cast irons.

The precipitation of Si-rich nitride in the diffusion zone of Si-alloyed steel has been extensively studied. Si is a so-called weak nitride forming element like Al and Mo,[20–23] exhibiting very slow precipitation kinetics in α-Fe as compared to strong nitride formers like Cr, V, and Ti.[23–25] At nitriding temperatures of < 580 °C, the Si-rich nitride precipitates are typically found to be amorphous.[18,26–29] The composition of the Si-rich nitrides being embedded in α-Fe was suggested to be Si$_3$N$_4$.[18,26] Recently it was, however, shown that the amorphous Si-rich nitride may contain a notable molar fraction of Fe when being embedded in ε (Table I).[19] In the following, Si-rich nitride embedded in both α-Fe or Fe nitride is denoted by X.

Si is known to affect the hardness and thickness of the compound layer,[5,30,31] and the hardness of the diffusion zone.[23,32] It is also known that Si might affect the nitriding conditions, under which the main iron nitrides ε and γ' form as compared to nitriding of pure iron. Upon nitriding Fe–1.0/2.3wt pctSi alloys, ε has been observed at nitriding conditions only allowing for the formation of γ' in pure α-Fe.[33,34] A higher Si solubility in ε as compared to a negligible solubility in γ' was assumed to promote the formation of ε. It seems uncertain whether the reported phase mixtures containing ε and γ' represent a state of equilibrium.*

---

*In the current work, the notion equilibrium refers to a state of *local metastable* equilibrium. At normal pressure, Fe nitrides are metastable with respect to N$_2$ gas. Phase equilibria are only fulfilled locally within the gradient of the N content between surface and substrate generated during nitriding.

---

nitriding Fe–3.5wt pctC–1.5/3wt pctSi alloys also at conditions only allowing for γ' formation in pure α-Fe, the current authors have shown that ε containing up to

STEFAN KANTE and ANDREAS LEINEWEBER are with the Institute of Materials Science, TU Bergakademie Freiberg, Gustav-Zeuner-Str. 5, 09599 Freiberg, Germany. Contact e-mail: andreas.leineweber@iww.tu-freiberg.de

1.5 at pct Si is the only Fe nitride forming from Si-enrich α-Fe.[19] This ε had grown in contact with α-Fe by means of a eutectoid transformation, α-Fe(Si) → ε + X, occurring upon increasing the chemical potential of N, and seemed to be stable against a transformation into γ′. Based on these findings for the Fe–C–Si–N system and in view of the above References 33 and 34, a schematic isothermal section of the Fe–Si–N phase diagram was proposed. In this phase diagram, the ε/γ′ phase boundary is shifted towards a lower chemical potential of N as compared to the Fe–Si–N phase diagram obtained from available thermodynamic databases of the Fe–Si–N system[35]. In nitrided Fe–C–Si alloys, however, ε might be also stabilized by C. Thus, an experimental proof of the proposed Fe–Si–N phase diagram is lacking.

Moreover, little is known about the formation sequence of ε and γ′ as well as the microstructure evolution of compound layers containing both nitrides in Fe–Si-base alloys.[30,34,36] Microstructure investigations were largely focused on γ′ in Si-rich ferrite. γ′ plates were observed, which protrude from the compound layer into the diffusion zone,[33,34,36–38] and which are referred to as *plate-type* γ′ in the present work. Moreover, a "tooth"-like morphology of γ′ has been described.[34] This "tooth"-like γ′ is composed of two Σ3-related γ′ grains which exhibit the Nishiyama–Wassermann orientation relationship (OR) with α-Fe (Table II). In contrast to "tooth"-like γ′, crystallographic features of the more frequently reported plate-type γ′ in Fe–Si alloys have not been studied. Similar to γ′ plates grown by a partially displacive transformation of N-supersaturated but otherwise pure α-Fe upon heat treating at < 250 °C, these plate-type γ′ might be related to α-Fe by a near-Pitsch OR.[39–41] Such near-Pitsch OR (Table II) governs also the early stage of γ′ growth during nitriding pure α-Fe, resulting in the formation of γ′ plates characterized by {0.08 4.3 9}$_α$||{3.9 3.7 8.4}$γ′$ habit planes.[42] For detailed information regarding the α/γ′ ORs, the reader is referred to the References 42 and 43.

The current work aims to provide a comprehensive image of the temporal evolution of the compound layer generated upon nitriding Fe–Si alloys. Crystallographic features of the Fe nitrides were studied by electron backscatter diffraction (EBSD), allowing to draw conclusions about the formation sequence and growth mechanism of ε and γ′. To clarify the effect of Si on the thermodynamic stabilities of ε and γ′, gas nitriding was conducted. Gas nitriding in NH_3/H_2-containing atmospheres allows thermodynamics-based control of the type Fe nitrides contained in the compound layer. The chemical potential of N, μ_N, at the material's surface and, thus, the nitride phase forming in contact with the nitriding atmosphere, can be adjusted by the partial pressures of NH_3 and H_2, p_{NH_3} and p_{H_2}, according to

$$\mu_N \propto \ln r_N, \qquad [1]$$

with

$$r_N = \frac{p_{NH_3}}{p_{H_2}^{3/2}} \qquad [2]$$

being the so-called *nitriding potential*.[49,50] In spite of the thermodynamics-based process control, also non-equilibrium microstructures may occur when kinetics constrain the phase transformations involved in the compound layer formation.

II. EXPERIMENTAL

An alloy of the composition Fe–3 wt pct Si was weighed in and produced by arc melting in Ar atmosphere, starting from pure Fe granules (99.98 pct) and Si lumps (99.9995 pct) supplied by *Alfa Aeser*. The Si content of the alloy determined by dissolution followed by inductively coupled plasma mass spectrometry was 2.8 wt pct, confirming the weighed-in composition. The alloy was cast into a Cu mold to produce a rod measuring 30 mm in length and 5 mm in diameter. The as-cast rod was sealed in a fused silica crucible in Ar atmosphere and homogenized at 900 °C for 2 hours. Nitriding was performed using specimens with a thickness of about 2 mm which were cut from the rod. These specimens were ground and polished (final step: 1 μm diamond suspension) prior to nitriding.

Gas nitriding was conducted in a laboratory-scale chamber furnace at 540 °C and a nitriding potential of 1 atm$^{-1/2}$ for 1, 4, 16, and 48 hours. These conditions are known to produce single-phase γ′ layers in pure α-Fe[51].**

**Pure Fe reference specimens were simultaneously nitrided with the Fe–3wt pctSi samples in order to assure that the observations made for the Fe–3wt pctSi alloy are due to Si and not affected by erroneous process control.

To terminate the nitriding treatment, the samples were pulled into the cold pre-chamber of the furnace, rinsed with cold process gas to assure fast cooling of the samples.

X-ray powder diffraction (XRD) measurements were carried out in the 2θ range of 30 to 125 deg at a step size of 0.01 deg, employing a *Bruker D8 ADVANCE* diffractometer operating with Co-K$_{α1}$ radiation. The diffraction patterns were evaluated using the software *TOPAS 5*,[52] in order to determine the type of Fe nitrides formed during nitriding. The crystallographic descriptions used for phase identification are given in Table II.

Metallographic cross sections were produced for microstructure investigations. For this, the samples were electrolytically coated with a protective Ni layer, embedded in *Struers Polyfast*®, ground, and polished (final step: *Buehler MasterMet*™ suspension). Scanning electron microscopy (SEM) and electron backscatter diffraction (EBSD) measurements were conducted using *JEOL JSM-7800f* equipped with the *EDAX Hikari Super* EBSD system and operated with an acceleration voltage of 20 kV. Backscatter electron (BSE) contrast

Table I. Description of the Crystalline Phases in the Nitrided Fe–3wt pctSi Alloy Based on Refs. [14] Through [17], Used to Index EBSD and XRD Patterns, As Well As of the Amorphous Si-Rich Nitride, X

Phase	Space Group	Typical Lattice Parameters	Description
α-Fe	$Im\overline{3}m$	$a = 2.866$ Å	body-centered cubic (bcc) Fe lattice
γ'-Fe$_4$N	$Pm\overline{3}m$	$a = 3.790$ Å	face-centered cubic (fcc) Fe lattice; N ordered in octahedral sites
ε-Fe$_3$N$_{1+x}$	$P6_322$	$a = 4.698$ Å, $c = 4.379$ Å[a]	hexagonal close-packed (hcp) Fe lattice; N/C ordered in octahedral sites; $-0.34 < x < 0.47$
X	—	—	amorphous Si or Fe–Si nitride; $(Si_3N_4)_{1-x}(Fe_3N_2)_x$; $x = 0$[18]; $0.33 < x < 0.43$[19]b

[a]The lattice parameters refer to a superstructure cell due to ordering of N with $a_\varepsilon = 3^{1/2}a_{hcp}$ and $c_\varepsilon = c_{hcp}$.
[b]x might depend on the nitriding conditions and the chemical potential of N. A possible homogeneity range is believed to include at least the values of $0 < x < 0.33$.[19]

Table II. Crystallographic Orientation Relationships (ORs) Between α-Fe and γ' As Well As α-Fe and ε Reported in the Literature and Relevant to the Current Study

Nishiyama–Wassermann OR[44,45]	Pitsch OR[39]	Near-Pitsch OR[42]	Burgers OR[46–48]
$(101)_\alpha \parallel (111)_{\gamma'}$	$(110)_\alpha \parallel (010)_{\gamma'}$	$(110)_\alpha \parallel (0.009\ 1\ \overline{0.132})_{\gamma'}$	$(101)_\alpha \parallel (0001)_\varepsilon$
$[11\overline{1}]_\alpha \parallel [10\overline{1}]_{\gamma'}$	$[1\overline{1}1]_\alpha \parallel [101]_{\gamma'}$	$[1\overline{1}1]_\alpha \parallel [1\ 0.091\ 0.757]_{\gamma'}$	$[11\overline{1}]_\alpha \parallel [1\overline{1}00]_\varepsilon$

The near-Pitsch OR, as presented here, was obtained based on the transformation matrix provided in Table 4 of Reference 42. The Burgers OR was originally proposed for the transformation of β-Zr into α-Zr.

was mainly used for imaging, which is Z-sensitive and gives dark contrast to the N-rich nitrides.

EBSD measurements were conducted using a step size of 50 nm. The quality of the EBSD patterns was occasionally low in the surface-adjacent part of the compound layer (compare Supplementary Figure S-1, refer to electronic supplementary material), particularly upon short nitriding time. Therefore, patterns were saved on a sample basis to validate and confirm the indexing by offline analysis with the *TSL OIM Analysis*[TM] *8.0* software. In doing so, the *neighboring pattern averaging and re-indexing* (*NPAR*[TM]) function[53] was used to reduce noise, improving the offline indexing in regions of poor pattern quality.

EBSD data were processed and plotted using the free *MATLAB*[TM] toolbox *MTEX*[54,55]. Crystallographic orientation relationships between α-Fe and the Fe nitrides were evaluated by pole figures analysis. In doing so, γ' and ε pole figures containing all possible variants of the ORs in Table II were calculated from experimental orientations of α-Fe *via MTEX*. γ' pole figures containing all variants of the near-Pitsch OR (black), the Pitsch OR (blue), and the Nishiyama–Wassermann OR (red) calculated from one given α-Fe orientation are shown Figure 1(a). The poles referring to each variant form different and well-distinguishable patterns. The pole figures calculated from experimental α-Fe orientations were superposed with the experimental orientation data of γ' and ε to determine the ORs and visualize the occurring variants. The data points were plotted semitransparently. The more data points overlap, and the more of the transparency is lost. By this, the approximate mean of the experimental orientations is highlighted while scatter and gradients in the orientations remain visible. The occurring variants of the ORs were numbered with

different colors, referring to the inverse pole figure (IPF) color coding[56] of ε and γ' given in Figure 1(b). The same color coding was applied in α-Fe, ε and γ' IPF maps with respect to the image plane normal in the figures of this work.

The poles referring to near-Pitsch OR and Pitsch OR variants in pole figures are close and related to each other, making it difficult to distinguish between these ORs by pole figure analysis if experimental orientation data are spread. Therefore, quantitative information on the goodness of fit of α/γ' ORs is provided in addition to the pole figures where necessary. For this, grains were calculated from the experimental EBSD data using *MTEX*.[54] Cumulative frequency distributions were obtained from the local α/γ' disorientations along the calculated grain boundaries, showing the frequency of occurrence of the ORs along the boundaries at a given angular deviation from the ideal ORs. The frequency distributions were normalized by the total number of α/γ' grain boundary segments evaluated in the regions of interest. For details on the interpretation of such frequency distributions, the reader is referred to Reference.[57]

The Vickers hardness (HV0.05) of the nitrided samples was measured on metallographic cross sections using a *Leica VMHT MOT* microhardness tester in order to trace changes in the hardness of α-Fe in the diffusion zone, being indicative of the progress of the precipitation of X in α-Fe. Hardness-depth profiles were measured with a step-width of 10 μm and a zig-zag pattern, ensuring that the deformation fields due to the indents do not affect each other. In addition, the hardness of the diffusion zone was measured parallel to the nitrided surface across the entire sample at a distance of 50 μm from the surface, using a step-width of 100 μm.
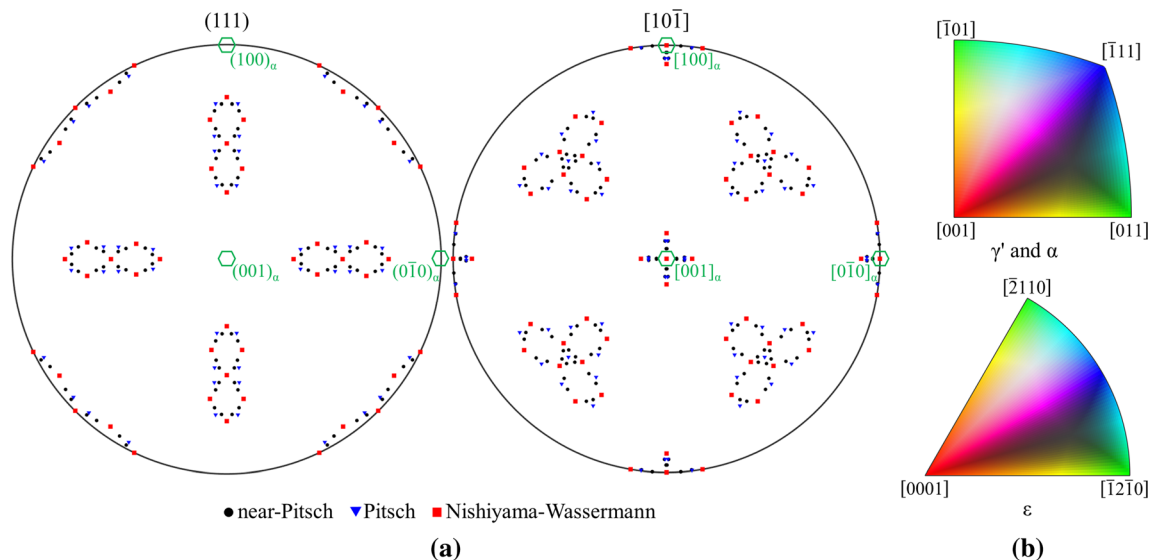
Fig. 1—(a) (111) and [10$\bar{1}$] pole figures of γ', projected onto a (100) pole figure of α-Fe, showing all variants of the near-Pitsch, Pitsch, and Nishiyama–Wassermann OR (Table II), calculated from a given α-Fe orientation using MTEX. (b) Color coding according to Ref. [56] used to color IPF maps of α-Fe, ε and γ' and to number variants in pole figures (Color figure online).
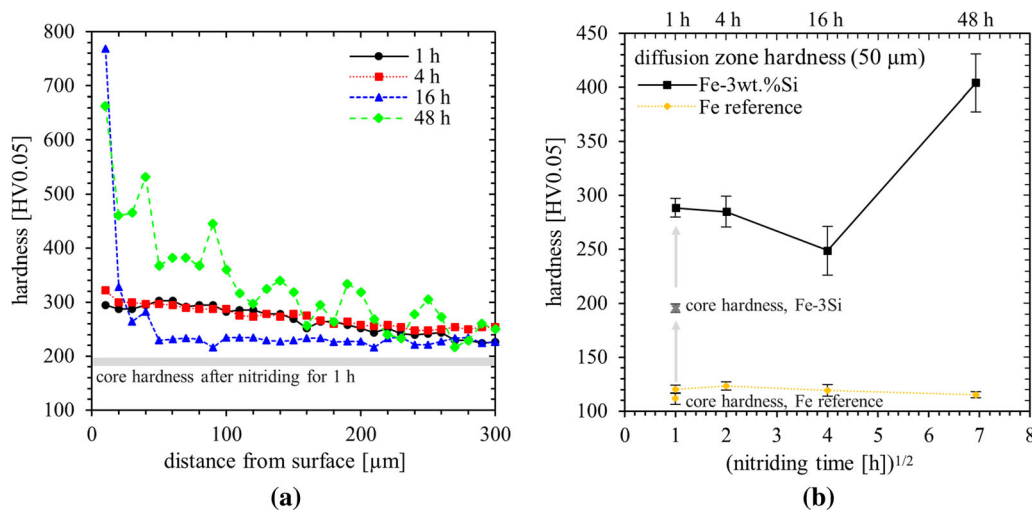

Fig. 2—(a) Hardness-depth profiles measured on the metallographic cross sections of Fe–3wt pctSi specimens after nitriding at $r_N = 1$ atm$^{-1/2}$ and 540 °C for 1 to 48 hours. Spikes in the hardness-depth profile obtained from the specimen nitrided for 48 hours may be due to the pronounced precipitation of X and of Fe nitride at (sub)grain boundaries. (b) Averaged hardness of the diffusion zone in nitrided Fe–3wt pctSi specimens and equally nitrided Fe reference specimens, measured at a distance of 50 μm from the surface, comprising data obtained from several α-Fe grains. The hardness measured in the still unnitrided core of a Fe–3wt pctSi specimen nitrided for 1 hour and in the core of a pure Fe reference specimen nitrided for 1 hour are shown for comparison.

III. RESULTS

A. Hardness

Hardness-depth profiles up to a distance of about 300 μm from surface obtained after nitriding for 1 to 48 hours are shown in Figure 2(a). In addition, the hardness measured in the core of a Fe–3wt pctSi specimen after nitriding for 1 hour, which is still unaffected by nitriding, is indicated for comparison. After 1 hour, the hardness of the diffusion zone has already increased with respect to unnitrided core. The hardness-depth profile obtained after 4 hours seems to

compare with the profile measured after 1 hour. After nitriding for 16 hours, the hardness is high at the surface but readily becomes lower as compared to 1 and 4 hours. Finally, the hardness of the diffusion zone is notably higher as compared to nitriding for 1 to 16 hours after 48 hours. The spikes in the hardness-depth profile after 48 hours may relate to measurement points affected by the precipitation of Fe nitride along subgrain boundaries. Besides, it is noted that the hardness values measured at a distance of < 20 μm from the surface in Figure 2(a) may be affected by the presence of the compound layer. This particularly pertains to specimens

nitrided for 16 to 48 hours, in which the hardness at a distance of < 20 μm from the surface is remarkably higher as compared to the hardness of the diffusion zone.

As the hardness-depth profiles mainly represent data obtained only from single α-Fe grains due to the coarse-grained samples, additional hardness measurements were conducted parallel to the surface at a distance of about 50 μm from the surface across the entire samples. The resulting mean values, comprising data obtained from various α-Fe grains, are shown in Figure 2(b). Note that spikes in the hardness associated with Fe nitride at (sub)grain boundaries were excluded from the data. The hardness values measured at 50 μm distance from the surface confirm the hardness evolution with time revealed by the hardness-depth profiles. The hardness has readily increased after 1 hour, then decreases, and finally increases again after 48 hours. The increase in the diffusion zone hardness of the Fe–3wt pctSi alloy upon nitriding is notably larger than the increase in the diffusion zone hardness of equally nitrided pure Fe (Figure 2(b)).

B. SEM

1. Precipitation of X in α-Fe

X typically appears as dark points or veins in BSE-contrast images.[19] X is not or hardly visible in SEM images of α-Fe in the diffusion zone after nitriding for 1 and 4 hours. X formed in α-Fe during short nitriding times might be mainly too small to be resolved by SEM-BSE imaging. Occasionally, clusters of X exist very locally in the proximity of the compound layer in the specimen nitrided for 4 hours. After nitriding for 16 hours, a large number density of X precipitates is often visible adjacent to the compound layer, however, readily decreases with increasing distance from the compound layer (Figure 3(a)). A very large number density of X precipitates is observed both adjacent to the compound and homogenously distributed in the bulk of α-Fe grains in the diffusion zone after nitriding for 48 hours (Figure 3(b)).
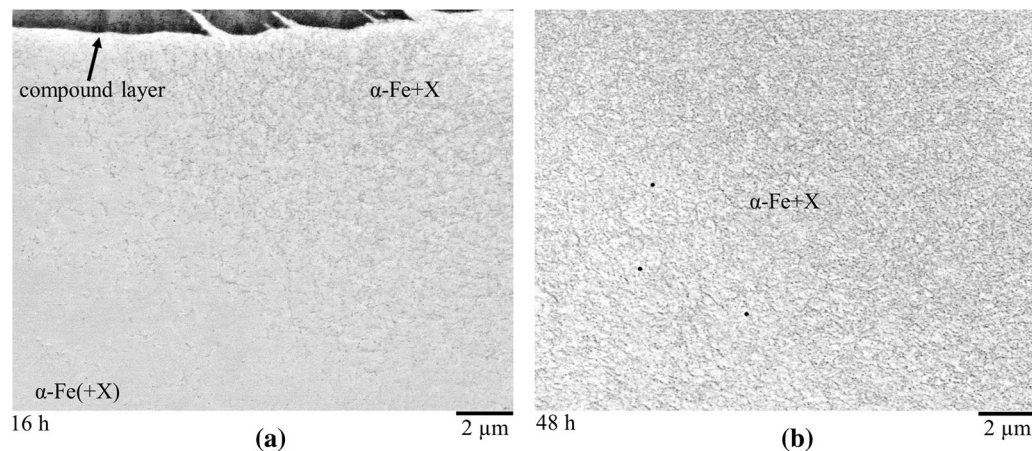
2. Microstructure of the compound layer

Figures 4(a) through (d) provides representative SEM images of the compound layers after nitriding for 1 to 48 hours, showing the evolution of the compound layer morphology with increasing time. The minimum and maximum compound layer thickness after different nitriding times, measured as indicated in Figures 4(a) through (d), are given in Figure 4(e). A dense nitride layer measuring about 1 μm in thickness has formed at the surface and at surface-adjacent grain boundaries after nitriding for 1 hour (Figure 4(a)). This layer is indistinct and blurred in BSE-contrast images due to its very fine structure. Occasionally, fine plate/lath structures could be resolved within that *dense compound layer* (Figure 4(f)). From the dense compound layer, thin nitride plates protrude into α-Fe. The plates measure several microns in length but typically less than about 50 nm in width.

The compound layer appears very serrated after nitriding for 4 hours (Figure 4(b)). The length of the nitride plates has increased, and they have become slightly thicker than the plates visible in the specimen nitrided for 1 hour. The difference in the thickness of the dense compound layer and the penetration depth of the nitride plates has increased (Figure 4(e)). Frequently, a midrib exists in the center of the nitride plates (Figure 4(g)), analogous to the midrib of martensite plates as reported for γ' plates formed in pure α-Fe.[42]

After nitriding for 16 and 48 hours, the compound layer growth seems to be preceded rather by conventional planar-type growth than by the protrusion of nitride plates into α-Fe (Figures 4(c) and (d)). Neighboring nitride plates have largely impinged due to lateral thickening. Therefore, the serrated morphology of the compound layer observed after 4 hour has diminished, and the thickness of the dense part of the compound layer has notably increased as compared to the specimen nitrided for 4 hours (Figure 4(e)). Thus, the minimum and maximum compound layer thickness approach each other. After impingement, the midribs of the nitride plates still reveal the original positions of the plates in the initial stage of nitriding (broken arrows Figure 4(h)).
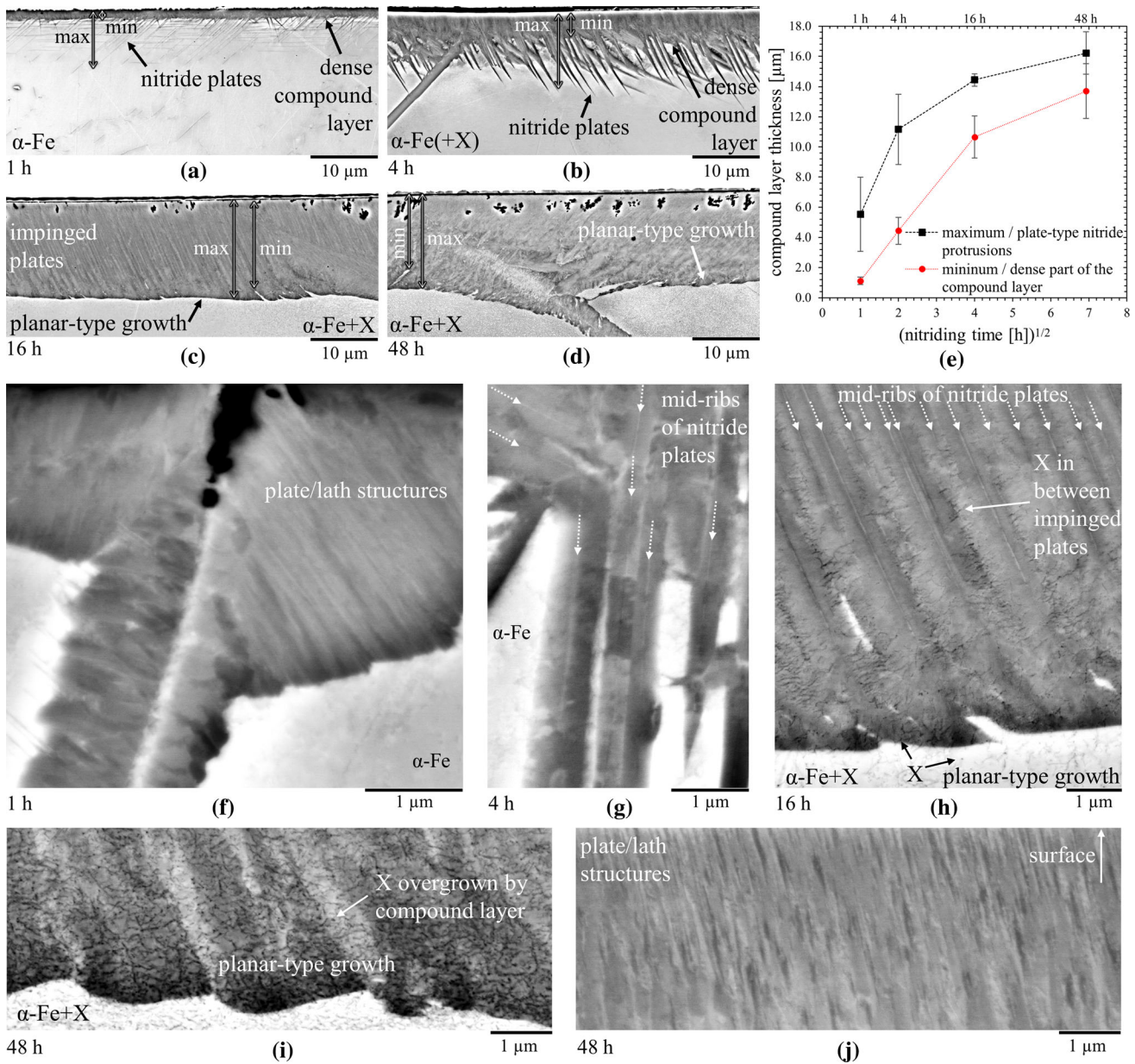

Fig. 3—BSE images of Fe–3wt pctSi specimens nitrided at r_N = 1 atm$^{-1/2}$ and 540 °C, showing the distribution of visible X precipitates in α-Fe in the diffusion zone (*a*) adjacent to the compound layer after nitriding for 16 h, and (*b*) at a distance of about 30 to 45 μm from the surface after nitriding for 48 h.

Fig. 4—(a) through (d) BSE images of metallographic cross sections of Fe–3wt pctSi specimens nitrided at r_N = 1 atm$^{-1/2}$ and 540 °C for 1 to 48 h. (e) Mean minimum and maximum compound layer thickness after different nitriding times, obtained as indicated in (a) through (d). The minimum thickness refers to the smallest thickness, up to which the compound layer appeared *dense* in a given α-Fe. The maximum thickness refers to the largest thickness of the compound layer, given by the maximum penetration depth of the nitride plates into the substrate during short nitriding time and being related to position of the growth front compound layer advancing by planar-type growth after prolonged nitriding. For each minimum and maximum thickness, three measurements were conducted per α-Fe grain. The values obtained from different grains were averaged. Large standard deviations result from α-Fe-grain-depended variations in the penetration depth of the nitride plates and the compound layer thickness. (f) through (j) BSE images of microstructural details in the compound layers after nitriding for 1 to 48 h; see text.

X is observed in the impingement zone between the plates. Possibly, Si is pushed aside with the advancing interface until precipitation takes place. Furthermore, X precipitated in α-Fe underneath the compound layer is overgrown *by* and incorporated *into* the compound layer advancing by planar-type growth (Figure 4(i)). The very fine plate/lath structures already observed in the compound layer after nitriding 1 hour, see above, are still visible in the surface-adjacent compound layer after 48 hours (Figure 4(j)).

C. *EBSD*

1. *Identification and crystallographic features of the nitride plates—plate-type γ′*

Section III–B has revealed nitride plates protruding from the dense compound layer into α-Fe in the early stage of nitriding. The plates exhibit different but distinct inclination angles with respect to the surface in given α-Fe grains, even though plates of a particular inclination angle seem to predominate in given α-Fe grains (Figures 5(a) and (b)). After nitriding for 1 hour,

no EBSD data can be obtained from the plates due to limited spatial resolution. Instead, only surrounding α-Fe is indexed (Figure 5(c)). Straight boundary traces suggest that the nitride plates have grown with specific habit planes, which can be determined based on EBSD data with respect to α-Fe. The boundary traces of the plates agree with $\{0.08 \ 4.3 \ 9\}_\alpha$ as habit plane (Figure 5(d)), i.e., the habit plane associated with the near-Pitsch OR.[42] Hence, the nitride plates observed after 1 hour most likely consist of γ' and exhibit the near-Pitsch OR with α-Fe. The microstructure observed after 1 hour is, therefore, considered to represent an early stage of the plate-type growth of γ' frequently reported upon nitriding Fe–Si alloys.[33,34,37]

EBSD patterns can be obtained from the γ' plates due to slight thickening of the plates after nitriding for 4 hours, confirming that they are composed of γ' (Figure 6(a)). Pole figure analysis indicates that the plates are related to adjacent α-Fe by the near-Pitsch OR (Figure 6(b)), as suggested above. The frequency distribution of the occurrence of α/γ' ORs (Figure 6(c)) at the α/γ' phase boundaries of the γ' plates in Figure 6(a) quantitatively supports this finding. The near-Pitsch OR fits slightly better with the experimental α/γ' disorientations than the closely related Pitsch OR, and significantly better than the Nishiyama–Wassermann OR. Definite distinction of the near-Pitsch and the Pitsch OR is difficult in view of the quality of EBSD patterns obtained from γ' plates and, thus, a possibly limited accuracy and precision of orientation determination. However, the literature has shown by means of the phenomenological theory of martensite crystallography that the near-Pitsch OR correctly describes the OR between γ' plates and α-Fe in nitrided and heat-treated

pure Fe.[40–43] Therefore, the Pitsch OR will not be further addressed in the following.

γ' plates which are related to α-Fe by different variants of the near-Pitsch OR often seem to incline the same angle with respect to the surface (Figure 6(a)). In general, this can be explained by the existence of near-Pitsch OR variant pairs exhibiting $\{\pm 0.08 \ 4.3 \ 9\}_\alpha$ habit planes nearby a common $\{049\}_\alpha$ plane.[40–43] Depending on the crystallographic orientation of α-Fe, the boundary traces of these habit planes and, thus, the inclination of the γ' plates with respect to the surface can be hardly distinguished in metallographic cross sections. Figure 6 shows a special case. Here, the surface normal of the specimen is approximately parallel to $[100]_\alpha$. There are consequently eight possible planes, $(\pm 0.08 \ 4.3 \ 9)_\alpha$, $(\pm 0.08 \ 4.3 \ 9)_\alpha$, $(\pm 0.08 \ 9 \ 4.3)_\alpha$, $(\pm 0.08 \ \overline{4.3} \ 9)_\alpha$, and $(\pm 0.08 \ \overline{9} \ 4.3)_\alpha$, referring to four near-Pitsch OR variant pairs, which approximately contain this $[100]_\alpha$ direction and, hence, also the specimen surface normal. The γ' plates referring to these variants and the boundary traces of their habit planes are, therefore, aligned more or less perpendicular to the specimen surface and practically indistinguishable in the cross-sectional image of the specimen. Five of those variants are visible in Figure 6(a). The variants 1 and 2 as well as 3 and 4 refer to variant pairs as described above. Occasionally, one variant changes to the other variant of a pair within a γ' plate, i.e., $1 \rightarrow 2$ and $3 \rightarrow 4$. This results in a small-angle grain boundary and can be assigned to the accomodation of transformation-induced strain.[40,42]

Figure 7(a) shows γ' which has grown with the "tooth"-like morphology reported for the nitrided Fe–Si alloys in Reference 34, introduced in Section I. This "tooth"-like morphology has been observed only in very
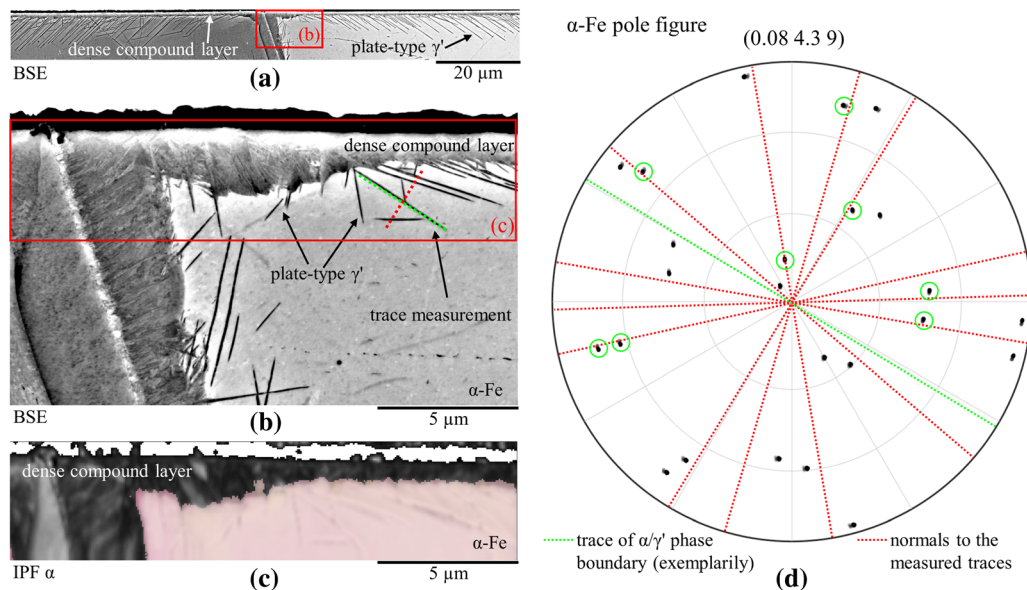

Fig. 5—(a) BSE overview image of the Fe–3wt pctSi specimen nitrided at $r_N = 1 \ atm^{-1/2}$ and 540 °C for 1 h, showing the compound layer in two α-Fe grains. (b) Close-up of the highlighted region in (a). (c) α-Fe IPF map of the highlighted region in (b). (d) Pole figure of α-Fe used for trace analysis of seven differently oriented γ' plates in (b). The boundary traces were measured in (b) and superposed to the pole figure (d), as exemplarily indicated by the green broken lines in (b) and (d). Then, the normals to the traces were drawn, red broken lines in (d). All trace normals approximately intersect with (0.08 4.3 9) poles, highlighted by green circles (Color figure online).
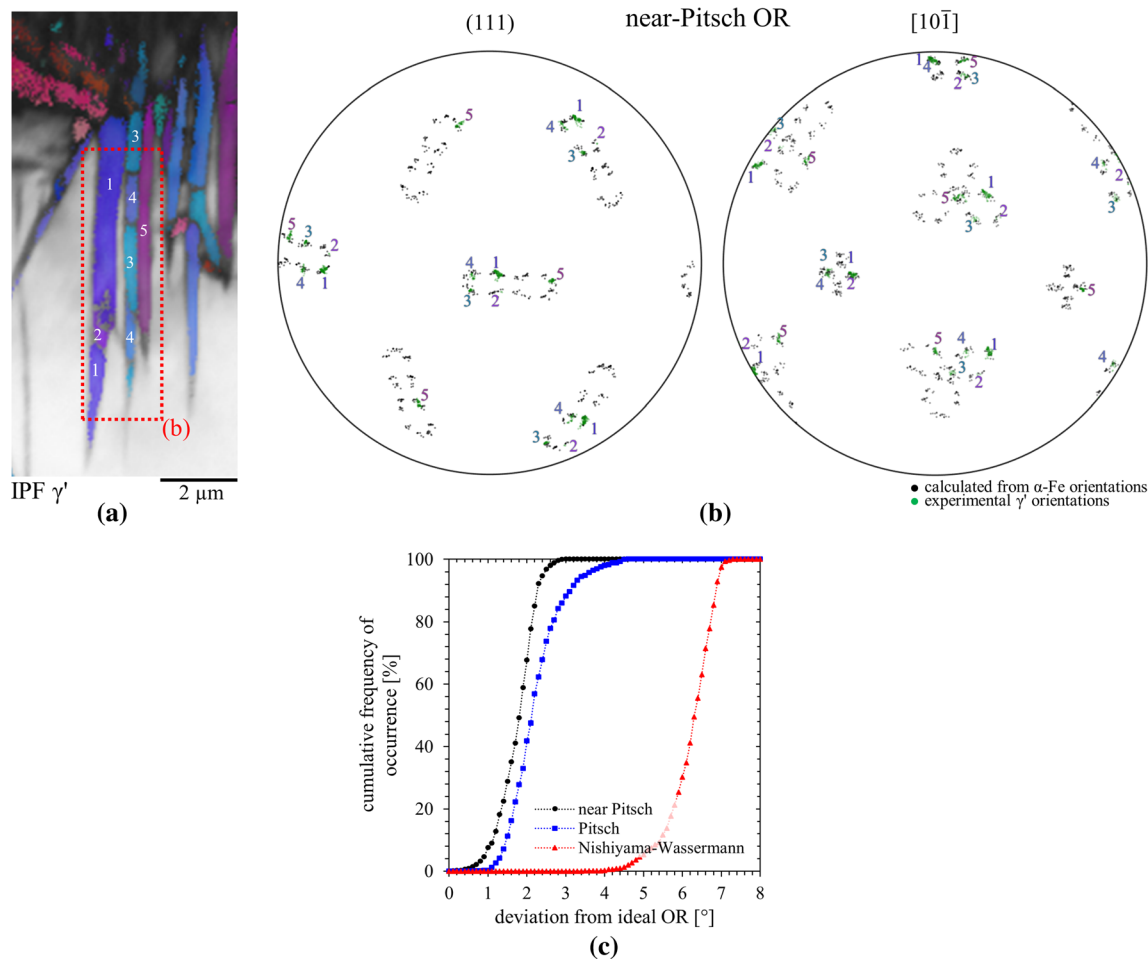
Fig. 6—(a) γ′ IPF map of γ′ plates grown in a Fe–3wt pctSi specimen nitrided at r_N = 1 atm$^{-1/2}$ and 540 °C for 4 h. (b) γ′ pole figures showing the position of all variants of the near-Pitsch OR (black) calculated from experimental α-Fe orientations in the highlighted region in (a), superposed with the experimental γ′ orientations (green) in the highlighted region. The experimental γ′ orientations agree well with five of the calculated near-Pitsch OR variants. (c) Cumulative frequency distribution revealing the occurrence of α/γ′ ORs at α/γ′ phase boundaries in the highlighted region in (a) at given angular deviation from the ideal ORs.

minor amounts in the present study. Agreeing with the Reference 34, the "tooth"-like γ′ is composed of two approximately Σ3-related γ′ grains exhibiting the Nishiyama–Wassermann OR with α-Fe (Figures 7(b) and (c)). Therefore, the crystallographic nature of the plate-type γ′ morphology, predominantly occurring in the present microstructures, intrinsically differs from the crystallographic nature of the "tooth"-like γ′ morphology characterized in the Reference 34.

2. Distribution of Fe nitrides in the dense part of the compound layer

EBSD has revealed the existence of ε and γ′ in the dense part of the compound layer after all nitriding times, also being confirmed by XRD measurements in Supplementary Fig. S-2a. Both ε and γ′ have formed at the surface and at grain boundaries, and both are in contact with the α-Fe after nitriding for 1 and 4 hours (Figures 8(a) and (b)). The phase fractions of ε and γ′ seem to differ among different α-Fe grains and α-Fe grain boundaries. At the α-Fe grain boundary seen in Figure 8(b), for instance, ε has formed in the

grain to the right, whereas γ′ has formed in the grain to the left.

While the compound layer contains a laterally heterogeneous distribution of ε and γ′ after short nitriding times, 1 and 4 hours, rather a multi-layer structure is observed after nitriding for 16 and 48 hours. ε exists only adjacent to the surface and is always separated from α-Fe by a γ′ sublayer (Figures 9(a) and (b)). This γ′ sublayer typically contains impinged γ′ plates in the center of the compound layer, and γ′ formed from α + X by planar-type growth, see the microstructure investigations in Section III–B. The phase fractions of ε and γ′ in the compound layer still vary among different α-Fe grains after nitriding for 16 and 48 hours.

Besides, Figures 9(a) and (b) reveals that ε and γ′ have formed *on top* of the original sample surface. The formation of such *surface nitrides* is related to stress release[58,59] and known from nitriding of white-solidified cast irons[19,60] and Fe–Al alloys.[61–63] The coverage of the surface with surface nitrides varies among different α-Fe grains, however, they do not form a dense surface layer even upon nitriding for 48 hours.
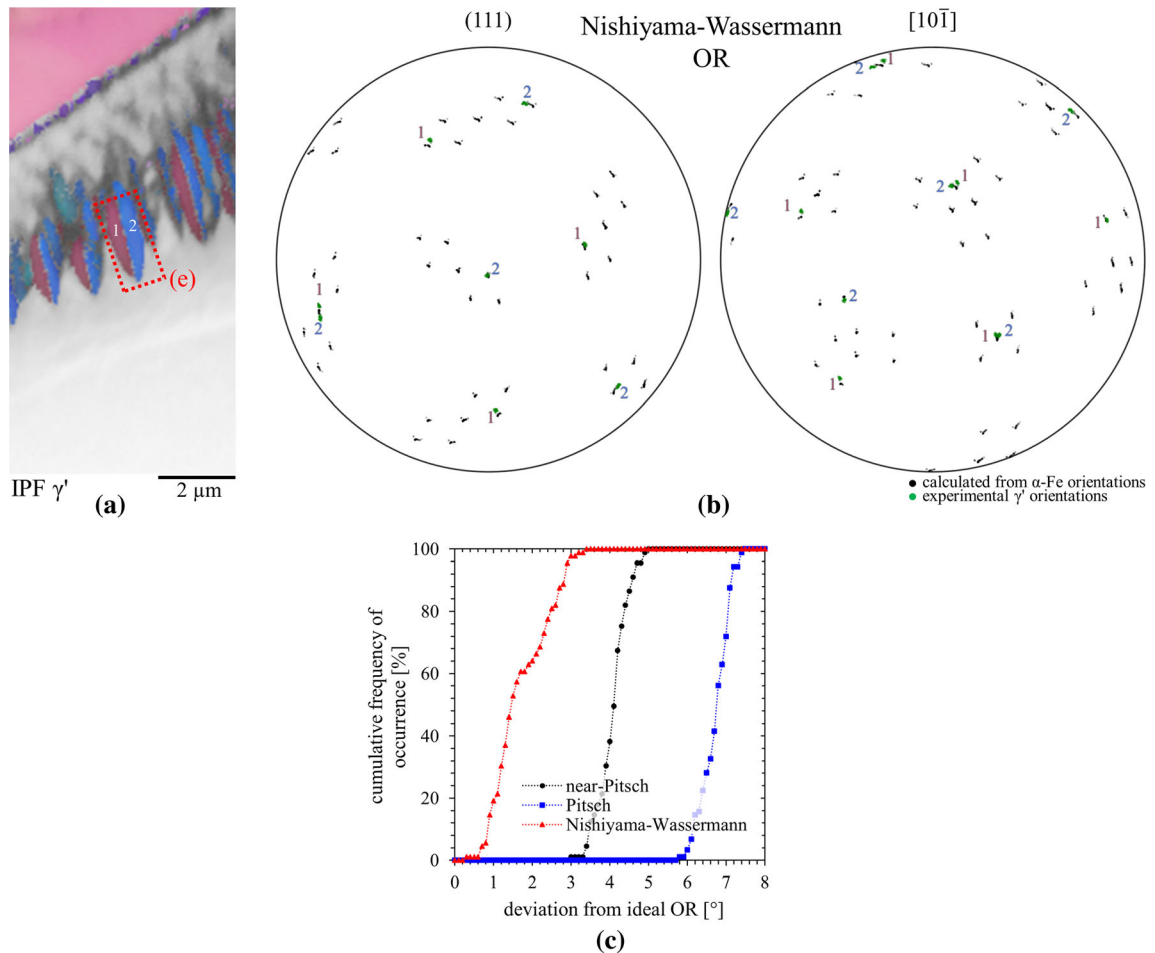
Fig. 7—(a) γ' IPF map of "tooth"-like γ' at a grain boundary in a Fe–3wt pctSi specimen nitrided at r_N = 1 atm$^{-1/2}$ and 540 °C for 4 h. (b) γ' pole figures showing the position of all variants of the Nishiyama–Wassermann OR (black) calculated from experimental α-Fe orientations in the highlighted region in (a), superposed with the experimental γ' orientations (green) in the highlighted region. The experimental γ' orientations agree well with two of the calculated Nishiyama–Wassermann OR variants, which are approximately Σ3-related. (c) Cumulative frequency distribution revealing the occurrence of α/γ' ORs at α/γ' phase boundaries in the highlighted region in (a) at given angular deviation from the ideal ORs.

3. *Crystallographic relationships between ε and γ' in the dense part of the compound layer and α-Fe*

As shown for the γ' plates in Section III–C–1, the near-Pitsch OR is mainly held between γ' in the dense part of the compound layer and α-Fe after nitriding for 1 and 4 hours (Figures 8(c) and (d)). Similarly, ε growing in contact with α-Fe almost invariably is related to α-Fe by the well-known Burgers OR[46] given in Table II (Figure 8(e)). That OR was previously observed for α-Fe precipitated in ε.[47,48] After nitriding for 16 and 48 hours, ε—now being separated from α-Fe by a γ' sublayer—still approximately exhibits the Burgers OR with underlying α-Fe in the diffusion zone (Figures 9(c) and (d)).

Similar to the occurrence of the Burgers OR between surface-adjacent ε and α-Fe of the diffusion zone, impinged γ' plates *inside* the compound layer, being separated from α-Fe by planar-type γ', are still related to α-Fe underneath the compound layer by the near-Pitsch OR (Figures 10(a) and (b)). Note that the presence of impinged γ' plates in the middle of the compound layer

in Figure 10 is revealed by their characteristic midribs (Section III–B–2). These midribs have the same inclination angle with the surface. The two variants of the near-Pitsch OR in Figure 10(b) refer to a variant pair as introduced in Section III–C–1. The interested reader is referred to Figure 4(h), showing a close-up of the microstructure in the region of the EBSD map in Figure 10(a).

γ' which is in contact with α-Fe in Figure 10 has formed by planar-type growth at the expense of α-Fe + X, see Figure 9(a). In contrast to impinged γ' plates *inside* the compound layer, the OR between γ' formed by planar-type growth and α-Fe is less clear from pole figure analysis. The experimental γ' orientations obtained from the region of the α/γ' phase boundary indicated in Figure 10(a) seem to be spread between the near-Pitsch OR and the Nishiyama–Wassermann OR (Figure 10(c)). The analysis of local α/γ' disorientations along the phase boundary via *MTEX* indicates that the near-Pitsch OR occurs at some parts of the phase boundary, while the Nishiyama–Wassermann OR
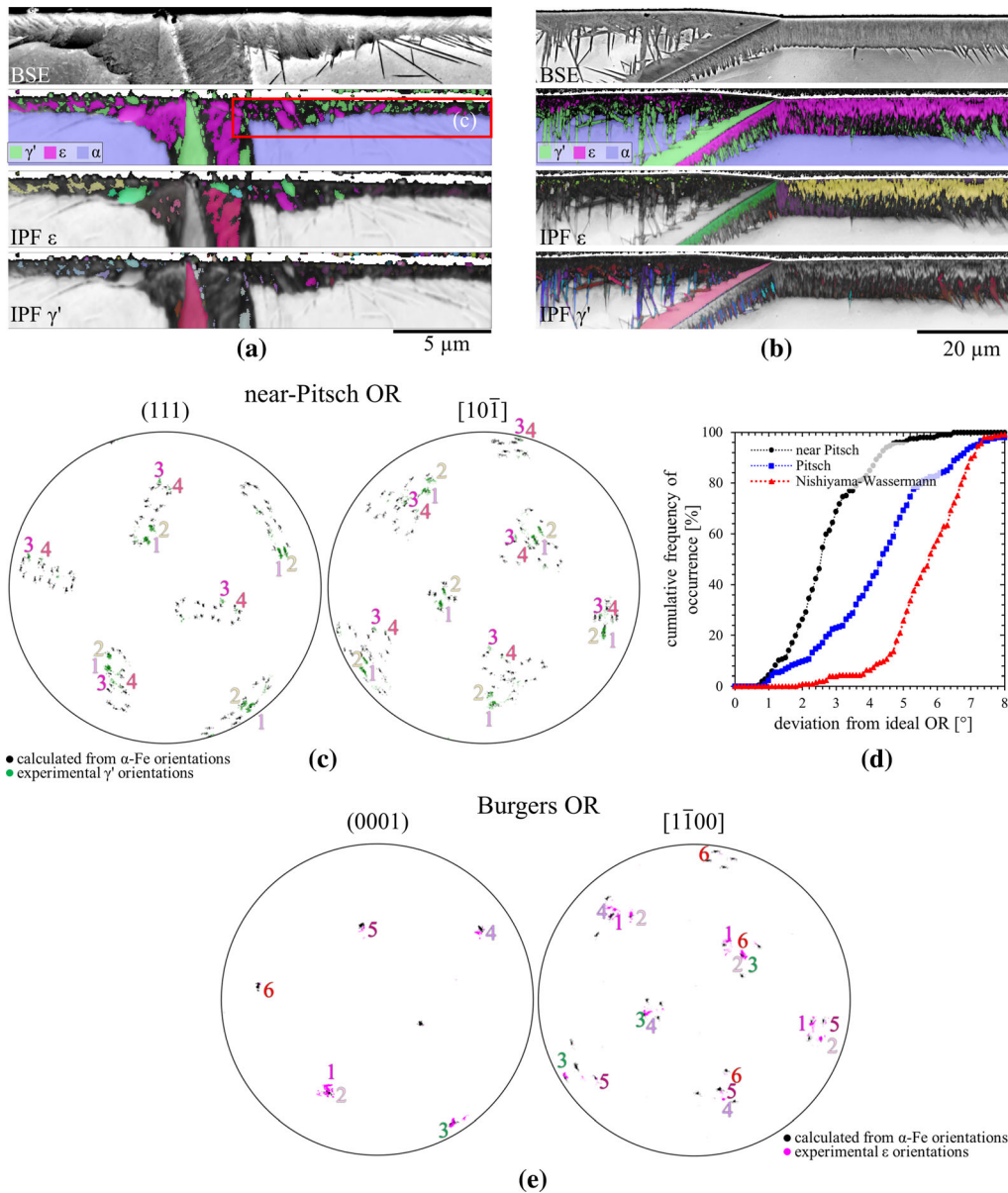
Fig. 8—BSE image and corresponding EBSD phase map, ε IPF map, and γ′ IPF map of Fe–3wt pctSi specimens nitrided at r_N = 1 atm$^{-1/2}$ and 540 °C for (*a*) 1 h and (*b*) 4 h. (*c*) γ′ pole figures showing the position of all variants of the near-Pitsch OR (black) calculated from experimental α-Fe orientations in the highlighted region in (a), superposed with the experimental γ′ orientations (green) in the highlighted region. The experimental γ′ orientations agree well with four of the calculated near-Pitsch OR variants. (*d*) Cumulative frequency distribution revealing the occurrence of α/γ′ ORs at α/γ′ phase boundaries in the highlighted region in (a) at given angular deviation from the ideal ORs, and confirming the result of pole figure analysis. (*e*) ε pole figures showing the position of all variants of the Burgers OR (black) calculated from experimental α-Fe orientations in the highlighted region in (a), superposed with the experimental ε orientations (magenta) in the highlighted region. The experimental ε orientations agree well with six of the calculated Burgers OR variants.

occurs at other parts, highlighted by yellow and red color in Figure 10(a). It appears that the planar-type γ′ forming upon prolonged nitriding has inherited the near-Pitsch OR from the above, initially formed γ′ plates, however the near-Pitsch OR is gradually lost during growth. The Nishiyama–Wassermann OR, then, might be observed by chance since it is close to the near-Pitsch OR. On the other hand, the present results could also indicate a transition from the near-Pitsch to the Nishiyama–Wassermann OR, which was recently reported for the initial growth of γ′ in pure Fe and

explained within the phenomenological theory of martensite crystallography in terms of a change in the slip direction of the line-invariant strain.[43]

IV. DISCUSSION

A. *Precipitation of X in α-Fe and Non-monotonous Hardness Evolution*

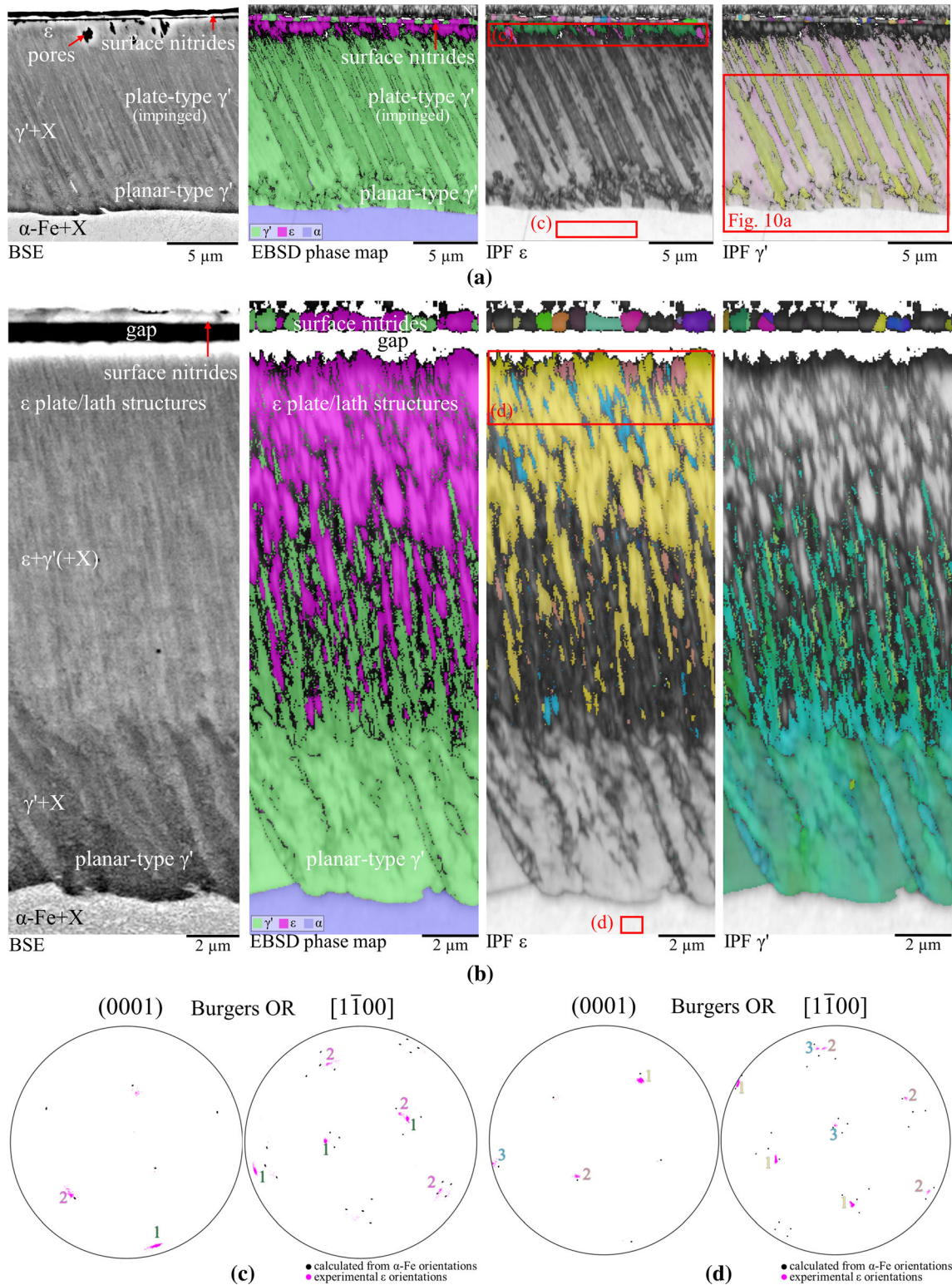The hardness measurements in Section III–A have revealed a non-monotonous evolution of the diffusion

Fig. 9—BSE image and corresponding EBSD phase map, ε IPF map, and γ′ IPF map of Fe–3wt pctSi specimens nitrided at r_N = 1 atm$^{-1/2}$ and 540 °C for (*a*) 16 h and (*b*) 48 h. Note the formation of ε and γ′ *surface nitrides* on top of the original sample surfaces. In (b), the surface nitrides got detached from the surface during sample preparation, resulting in a gap. A close-up BSE image of microstructure in the surface-adjacent compound layer region in (b) is presented in Fig. 4(j). (*c* and *d*) ε pole figures showing the position of all variants of the Burgers OR (black) calculated from experimental α-Fe orientations underneath the compound layer in the highlighted region in (a) and (b), respectively, superposed with the experimental ε orientations in the highlighted region in the surface-adjacent compound layer (magenta). The experimental ε orientations approximately agree with the calculated Burgers OR variants.
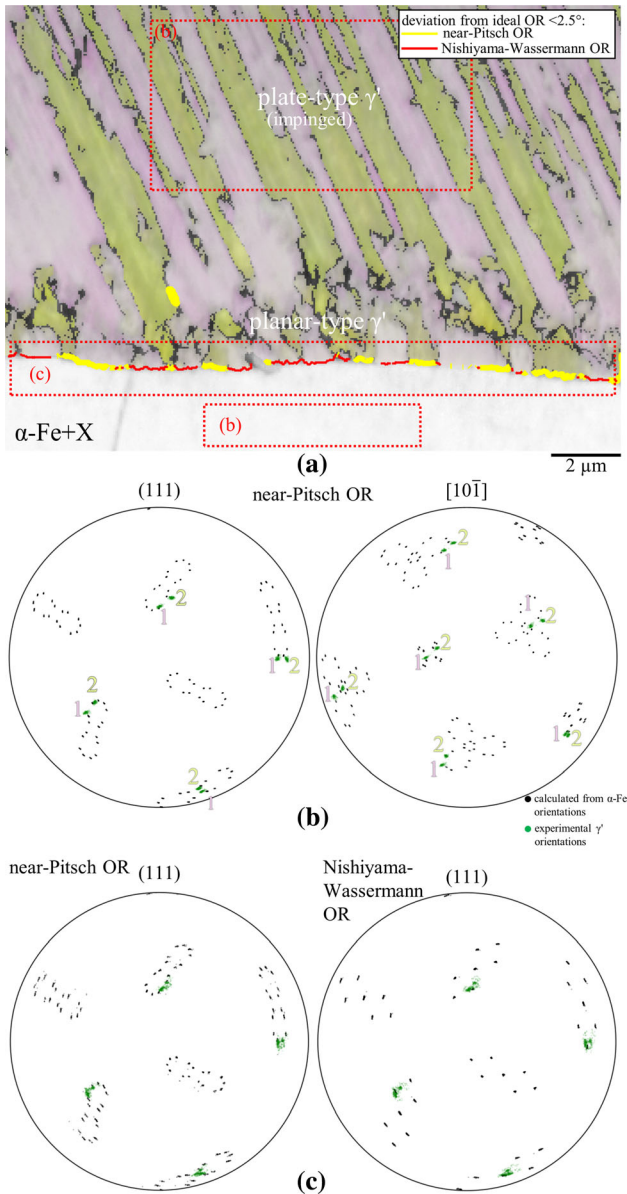
Fig. 10—γ' IPF map of a Fe–3wt pctSi specimen nitrided at $r_N = 1$ atm$^{-1/2}$ and 540 °C for 48 h, preproduced from Figure 9(a). Note that a close-up BSE image of the microstructure in the region of the IPF map is provided in Fig. 4(h). Parts of the α/γ' phase boundary are highlighted, at which the near-Pitsch and the Nishiyama–Wassermann OR are fulfilled within an angular deviation of < 2.5 deg from the ideal ORs. (b) γ' pole figures showing the position of all variants of the near-Pitsch OR (black) calculated from experimental α-Fe orientations in the highlighted region underneath the compound layer in (a), superposed with the experimental γ' orientations of impinged γ' plates in the middle of the compound layer (green). The experimental γ' orientations agree well with two of the calculated near-Pitsch OR variants. (c) γ' pole figures showing the position of all variants of the near-Pitsch OR and of the Nishiyama–Wassermann OR (black) calculated from experimental α-Fe orientations in the highlighted region at the α/γ' phase boundary in (a), superposed with the experimental γ' orientations of planar-type γ' (green) in the respective region (Color figure online).

zone hardness with increasing nitriding time, as previously reported upon nitriding Fe–Si alloys.[23] The hardness first increases with respect to the unnitrided

core, then decreases and finally increases again (Figure 2). The increase in hardness after 1 hour is notably larger than expected from solid solution hardening due to the incorporation of N into α-Fe only, see the nitrided pure Fe reference in Figure 2(b). This strongly suggests that X has precipitated in α-Fe of the diffusion zone already after nitriding for 1 hour, even though it could not be resolved by SEM in Section III–B–1. Note that also the amount of N being dissolved in α-Fe in the nitrided Fe–3wt pctSi specimen and in the pure Fe reference specimen might be different, leading to different degrees of solid solution hardening.

The non-monotonous change of the diffusion zone hardness in nitrided Fe–Si alloys has been discussed and explained in Reference 23 as follows. Very fine X precipitates form in α-Fe upon short nitriding times, which are in line with the absence of visible X precipitates in α-Fe after 1 to 4 hours in the current work. The fine precipitates cause a first increase in hardness. Afterwards, the precipitates coarsen, leading to a decrease in hardness. After prolonged nitriding, new X precipitates form promoted by lattice defects induced by the plastic accommodation of the volume misfit between the initially formed and now coarsened X precipitates and the α-Fe matrix. The formation of new X precipitates causes the second increase in hardness. For the present work and subsequent discussions, it is important to recognize that the observed non-monotonous hardness evolution with nitriding time, therefore, implies that Si is not fully precipitated as X and still dissolved in α-Fe, particularly, during short nitriding times.†

---

† α-Fe lattice parameters estimated from XRD patterns in Supplementary Fig. S-2b substantiate that Si is still substitutionally dissolved in α-Fe after nitriding during short nitriding times.

B. Change of the Compound Layer Growth with Nitriding Time

The microstructure and growth morphology of the compound layer in the Fe–3wt pctSi alloy change with increasing nitriding time. The growth of γ' plates is prominent during short nitriding times, whereas a planar-type growth γ' is prominent after prolonged nitriding. In addition, the occurrence of ε and γ' in the compound layer changes with increasing nitriding time, which is schematically summarized in Table III. The change in the growth morphology of the compound layer after different times seems to correlate with the Si content of α-Fe, into which the Fe nitrides grow, and which changes over the nitriding time due to the successive precipitation of X, compare the hardness evolution in Section I. In the following, the mechanism of compound layer growth during different nitriding times is discussed with regard to the microstructure formation, the role of Si, and the establishment of local phase equilibria.

Table III. Sequence of Nitrides in the Compound Layer From Surface (Left) to Substrate (Right) After Nitriding the Fe–3wt pctSi Alloy at $r_N = 1$ atm$^{-1/2}$ and 540 °C, Based on SEM, EBSD and XRD Results

Nitriding Time (hours)	Phase Sequence
1	$\varepsilon + \gamma'/\alpha + X/\alpha$-Fe
4	ε or $\varepsilon + \gamma'/\alpha + X/\alpha$-Fe
16	ε or $\varepsilon + \gamma'/\gamma' + X/\alpha + X/\alpha$-Fe
48	ε or $\varepsilon + \gamma'/\gamma' + X/\alpha + X/\alpha$-Fe

1. Short nitriding times: partially displacive growth under conditions off-equilibrium

After short nitriding times, 1 and 4 hours, the precipitation of Si-rich nitride, X, in α-Fe is not terminated yet, indicated by SEM imaging and shown by hardness measurements in Sections III–A and III–B. Hence, it appears that the Fe nitrides are forced to grow into Si-supersaturated α-Fe. Here, Si-supersaturated means supersaturated with respect to the Si content dissolved in α-Fe in a state, in which the equilibrium amount of X has precipitated at the given temperature and chemical potential of N (also implying N-supersaturation of α-Fe; see Reference 34).

Both ε and γ' seem to have nucleated at the surface and grow at the expense of α-Fe simultaneously, implying the coexistence α/ε and α/γ' phase boundaries during nitriding for 1 and 4 hours. The α/ε phase boundaries are compatible neither with the accepted Fe–N and Fe–C–N phase diagrams[51,64] nor with existing thermodynamic databases of the Fe–Si–N system[35] at the employed nitriding temperature of 540 °C, which do not allow for local $\alpha + \varepsilon$ equilibrium. Furthermore, α/ε phase boundaries do not exist in the microstructure after nitriding for 16 and 48 hours. Therefore, and due to the non-terminated precipitation of X in α-Fe, the microstructures observed after nitriding for 1 and 4 hours very likely represent a state *off*-equilibrium. A *state off-equilibrium*, here, means that local equilibria are not established at all phase boundaries between the solid phases inside the entire microstructure. The type of deviation from local equilibrium requires knowledge on the local distribution and state of Si in the microstructure and, particularly, at α/ε and α/γ' interfaces, which needs to be addressed by future research.

The compound layer growth into Si-supersaturated α-Fe during short nitriding times is invariably governed by the occurrence of crystallographic ORs between α-Fe and both ε and γ', which are typical of partially displacive transformations. The near-Pitsch α/γ' OR, associated with the growth of γ' plates, is indicative for a displacive mechanism transforming the bcc Fe lattice of α-Fe into the fcc Fe lattice of γ' upon diffusional supply of N.[40–43] Likewise, the Burgers OR—originally proposed for the transformation of bcc β-Zr into hcp α-Zr[46] —indicates a shear-based transformation of the bcc Fe lattice of α-Fe into the hcp Fe sublattice of ε; compare the ε martensite $\rightarrow$ α'-martensite

transformation.[65] Plate or lath structures corroborating a partially displacive formation of ε were observed (Figure 4(f) and corresponding EBSD data in Supplementary Fig. S-3). It is concluded that a (partially) displacive transformation mechanism is involved, at least, in the initial formation of both ε and γ' from α-Fe(Si), as reported for the initial formation of γ' during nitriding pure α-Fe.[42,43] Note that, similarly, a "martensite-like" formation of γ' in nitrided Fe–Si alloys has also been suggested in Reference 34. Si appears to enhance the importance of such a transformation mechanism, affecting the microstructure and morphology of the compound layer, which is discussed in the subsequent Section I

2. Short nitriding times: the role of Si during initial compound layer growth

The effect of Si on the Fe nitride and compound layer formation from Si-supersaturated α-Fe during short nitriding times may be explained making three assumptions:

i. The Si solubility in Fe nitrides is low,[19,33] *i.e.*, Si partitioning is required for Fe nitride growth.
ii. The mobility of Si at the process temperature is limited, meaning that long-range redistribution is impeded during nitriding.
iii. The large chemical potential of N generated at the materials surface during nitriding induces a large driving force to transform α-Fe into Fe nitride.

Based on the assumptions (i–iii), the following is proposed. The initial formation of fine Fe nitride plates in Si-supersaturated α-Fe by a partially displacive mechanism is hardly obstructed by Si, as only short diffusion distances are required to redistribute or reject Si at the tip of the plates. Note the small thickness of the initial γ' plates, which protrude deeply into the material but measure less than 50 nm in width (Figures 5(a) and (b)). In addition, partially displacive growth may also lead to a forced incorporation of Si into the Fe nitrides, compare Reference 34, as suggested for the forced incorporation of Si into cementite precipitating during martensite tempering.[66,67] In this regard, a higher Si solubility in ε as compared to γ'[19,33,34] might promote a direct transformation of α-Fe into ε.

Once formed, lateral thickening of the Fe nitrides is likely impeded by Si (i + ii). Instead, as the driving force to transform α-Fe into Fe nitride is large (iii), repeated nucleation and growth of further Fe nitride by the partially displacive mechanism are promoted. A large number of nucleation events in the early stage of nitriding may result in a remarkable structural refinement of the compound layer in the Fe–3wt pctSi alloy (see Section III–B and fine plate/lath structures in Figures 4(f) and (j)) as compared to Si-free steels, in which compound layers typically contain ε or γ' grains measuring several microns in diameter. That fine microstructure is retained adjacent to the surface even upon prolonged nitriding, *e.g.*, Figure 4(j). X or Si enrichment at the boundaries of the initially formed Fe

nitride might obstruct coarsening of the γ' and ε grains in the compound layer.

The need of Si redistribution (i) may particularly hamper the growth of the dense part of the compound layer and lateral thickening of γ' plates due to (ii). The protrusion of single γ' plates into depth, by contrast, seems largely unobstructed by Si due to the small dimension of the plates at their tips (see above). As Si hampers the overall growth of the dense part of the compound layer, less of the inwards diffusing N might be consumed by Fe nitride formation as compared to unconstrained growth. The resulting excess of N diffuses into the substrate, where it may further promote the growth of the γ' plates into depth. Thereby, the serrated compound layer morphology results, which is partially retained even upon prolonged nitriding time when the growth of the γ' plates into depth has notably slowed down.

It is remarked that confirming the above-suggested effects of Si on the formation and growth of the Fe nitrides requires further investigations by transmission electron microscopy and atom probe tomography. These should clarify the distribution of Si and X ahead and beyond the growth front of the compound layer, and whether Si is contained in the Fe nitrides. In addition to the above-mentioned forced incorporation of Si into Fe nitride, partitioning of Si between Fe nitride and X might also occur directly the growth front of the compound layer, possibly resulting in the cooperative growth of Fe nitride + X. Such cooperative growth of ε + X at the expense of α-Fe(Si) is known from nitriding of white-solidified Fe–C–Si alloys.[19]‡

---

‡Very occasionally a eutectoid-like phase mixture containing ε was observed after nitriding for 1 hour (Supplementary Figure S-4) and ongoing TEM investigations indicate the presence of a large number density of finely dispersed precipitates in the compound layer in a specimen nitrided for 48 hours.

---

3. Variant selection and effect on compound layer morphology

The predominant occurrence of γ' plates exhibiting the same inclination angle with respect to the surface and referring to a near-Pitsch OR variant pairs (Section III–C–1) was frequently observed in given α-Fe grains. This predominant occurrence of particular near-Pitsch OR variants indicates that variant selection is involved in the partially displace formation of γ'. The reason for this variant selection could not be resolved yet; however, the variant selection causes notable variations in the macroscopic compound layer morphology and in the compound layer thickness among different α-Fe grains.

If the $\{\pm 0.08 \ 4.3 \ 9\}_\alpha$ habit planes of preferentially growing γ' plates are aligned perpendicular to the surface, the maximum compound layer thickness may be large and the compound layer appears strongly serrated. For small inclination between the habit plane and the sample surface, the maximum compound layer thickness is smaller and the compound layer appears

rather planar, as proposed based on the investigation of "tooth"-like γ'.[34] The variations in the compound layer morphology and thickness originating from the partially displace growth of γ' and variant selection are still prominent after prolonged nitriding, when the γ' plates have largely impinged and the plate-type growth of γ' is replace by planar-type growth.

4. Prolonged nitriding: compound layer advancing under local equilibrium

A large volume fraction of X is visible in α-Fe adjacent to the compound layer after nitriding for 16 hours and, in particular, after nitriding for 48 hours, as shown and discussed in Sections III–B–1 and I. Due to the pronounced precipitation of X in α-Fe, the Si content of α-Fe adjacent to the compound layer should be notably lower than after nitriding for 1 to 4 hours, possibly approaching its equilibrium value at given distance from the surface. As a consequence of Si being largely bound in X, residual Si in α-Fe may have no or lesser effect than during early stage nitriding on the Fe nitride formation. This is manifested in three observations.

First, the α/ε phase boundaries observed after 1 to 4 hours, being incompatible with thermodynamic descriptions and databases of the Fe–N, Fe–C–N, and Fe–Si–N systems,[35,51,64] are not visible anymore after 16 and 48 hours. Only α/γ' phase boundaries exist, as a γ' interlayer invariably separates α-Fe and ε (Table III). Second, compound layer growth is not preceded by the protrusion of γ' plates anymore but by planar-type growth of γ' (Section III–B–2), which is typical of nitriding pure Fe or low-alloyed steels. X precipitates formed in α-Fe are overgrown *by* and incorporated *into* this planar-type γ'. Third, the near-Pitsch α/γ' OR, which is characteristic of the partially displace transformation α-Fe into γ', appears to be less prominent or lost during the growth of the planar-type γ', see Section III–C–3. Thus, the partially displacive transformation mechanism, which is very important for the microstructure and compound layer formation during short nitriding times due to the Si supersaturation of α-Fe, becomes of minor importance with the successive depletion of α-Fe in Si upon increasing nitriding time.

From the changes in the growth morphology and mechanism of the compound layer as well as the disappearance of α/ε phase boundaries, it is inferred that the compound layer advances into Si-depleted α-Fe under conditions of local equilibrium or close to local equilibrium at the α/γ' phase boundaries after prolonged nitriding. It may be assumed that the compound layer after prolonged nitriding, therefore, might be mainly controlled by the inward diffusion of N, without any constraints due to limited rates of Si redistribution on Fe nitride growth. Note that the evolution of the compound layer thickness with time (Figure 4(e)) does not agree with a parabolic growth law, typical of N-diffusion-controlled compound layer growth, within the range of the investigated nitriding times due to the partially displacive growth mechanism involved in the Fe nitride formation during short nitriding times.

C. Stability of ε During Nitriding of the Fe–3wt pctSi Alloy

Upon nitriding of the present Fe–3wt pctSi alloy at 540 °C under conditions only allowing for the formation of γ' in α-Fe[51,64], ε was observed in contact with the nitriding atmosphere after all nitriding times (Table III). Note that, in pure Fe at 540 °C, stable ε can exist in contact with the nitriding atmosphere only at a larger nitriding potential (chemical potential of N) than the one applied in the present work.[51,64] The phase fraction of ε contained in the compound layer, however, seems to notably vary among different α-Fe grains. A minor phase fraction of ε has been revealed in some α-Fe grains by EBSD, whereas other α-Fe grains exhibit a distinct ε layer at the surface, e.g., Figures 6(b) and 9(b). After prolonged nitriding, this surface-adjacent ε is always separated from underlying α-Fe by a γ' interlayer, however, approximately exhibits the Burgers OR with underlying α-Fe, alike ε growing in direct contact with α-Fe during short nitriding times (Section III–C–3). This suggests that surface-adjacent ε visible in the compound layer has already formed in the beginning of the nitriding treatment in contact with both α-Fe and the nitriding atmosphere, and more importantly that this ε was retained in contact with the nitriding atmosphere upon prolonged nitriding.

The initial formation of ε in contact with the nitriding atmosphere at the present nitriding conditions might be rationalized by a Fe nitride formation under off-equilibrium conditions (compare discussion in Section I). Once formed, however, the persistence of ε against an eventual transformation into γ' under nitriding condition enforcing the formation of γ' in pure α-Fe is striking. Therefore, the present results provide first clear evidence that ε can be stable at a lower nitriding potential and, thus, at a lower chemical potential of N in the Fe–3wt pctSi alloy than in pure Fe within the limits of technologically reasonable nitriding times. This agrees with observations made for nitrided Fe–C–Si alloys.[19] In contrast to the latter, any ε-stabilizing effect due to the additional presence of C can be excluded in the present Fe–3wt pctSi alloy.

As the state and distribution of Si in the compound layer has not been clarified yet by the present investigations—which needs to be done in future work—the reason for the stability of ε in the nitrided Fe–3wt pctSi alloys remains uncertain. A dissolution of Si in ε, hypothesized for ε in nitrided Fe–Si alloys[33,34] and shown by the present authors for ε in nitrided Fe–C–Si alloys[19], could explain the stability of ε at a lower chemical potential of N than in pure Fe. If Si is contained in ε of the Fe–3wt pctSi alloy, future investigations must also clarify whether this Si in ε originates from an equilibrium Si solubility in ε, or whether Si is trapped in ε due to the partially displacive growth of ε in the early stage of nitriding, Section I. Besides, nanostructuring§[68]

---

§Consider the extremely fine plate/lath structures in ε formed by the partially displacive mechanism, which are retained upon prolonged nitriding; see Figure 4(j) and upper part of Figure 9(b).

or large compressive residual stresses[69] in the compound layer, being of at least partially hydrostatic character, could stabilize ε with respect to γ'.

In contrast to the Fe nitrides formed inside the Fe–3wt pctSi alloy, the Fe surface nitrides formed on top of the original sample surface (Section III–C–2, Figures 9(a) and (b)) should have grown undistorted, mainly controlled by the outward diffusion of Fe, compare References 58, 59, and 61. Therefore, a forced incorporation of Si into the surface nitrides due to a partially displacive growth mechanism can be excluded. Neither, the surface nitrides should be notably affected by compressive residual stresses, as they do not constitute a dense layer on the surface. Neither, they exhibit an internal nanostructure. Still, the surface nitrides are composed of both γ' and ε.

The formation of only γ' surface nitride is expected at the present nitriding conditions if the surface nitrides grow due to the outward diffusion of only Fe atoms. Such a situation has been observed in equally nitrided Fe–3.5wt pctC–1.5/3wt pctSi alloys.[19] In the latter, compound layer growth in Si-rich α-Fe involves the eutectoid reaction α-Fe(Si) → ε + X, such that Si can be assumed to be largely bound in X. Si might be less tightly bound in the compound layer of the current Fe–3wt pctSi alloy. Consequently, Si may diffuse out of the sample together with Fe and—if soluble in ε—promote the formation of ε on the surface. Note that a possible Si dissolution in ε surface nitride still needs to be experimentally validated. The observed formation of ε surface nitride, however, may substantiate that Si and different Si solubilities in ε and γ', indeed might stabilize ε with respect to γ' at given nitriding potential and, respectively, chemical potential of N. Such effect of Si on the stability ranges of ε and γ', then, should cause a shift of the γ'/ε phase boundary in the Fe–Si–N phase diagram towards a lower chemical potential of N (see above), which is not evident from available thermodynamic databases for the Fe–Si–N system but was previously hypothesized based on nitriding of Fe–C–Si alloys.[19]

V. CONCLUSIONS

A Fe–3wt pctSi alloy was nitrided at process conditions known to produce single-phase γ' layers in pure α-Fe, i.e., at 540 °C and $r_N = 1$ atm$^{-1/2}$, for different nitriding times. EBSD has revealed the distribution of Fe nitrides in the compound layer. The EBSD-based study of crystallographic ORs between α-Fe, ε and γ' has allowed for conclusions regarding the growth mechanism and formation sequence of the Fe nitrides. Valuable information on the effect of Si on the temporal evolution of the compound layer and the stability ε was obtained, which is relevant to nitriding treatments for steels and cast irons. The key findings are summarized as follows:

1. The hardness of the diffusion zone non-monotonously changes with increasing nitriding time. The incomplete precipitation of Si-rich nitride, X, leads

to a limited increase in hardness and Si supersaturation of α-Fe during short nitriding time. The pronounced precipitation of X after prolonged nitriding leads to a notable increase in the hardness from about 200 HV0.05 to about 400 HV0.05, and results in a depletion of α-Fe in Si.

2. During short nitriding times, ε and γ' simultaneously grow into Si-supersaturated α-Fe. The invariably occurrence of the Burgers α/ε OR and the near-Pitsch α/γ' OR indicate that a partially displacive transformation mechanisms is involved in the initial formation of ε and γ' from Si-supersaturated α-Fe. Si initially impeding growth of the Fe nitrides, in conjunction with the partially displacive growth mechanism and repeated re-nucleation of Fe nitride, may lead to a notable microstructure refinement in the surface-adjacent compound layer.

3. The compound layer growth during short nitriding times is led by the protrusion of γ' plates into the substrate. In given α-Fe grains, γ' plates referring to specific pairs of near-Pitsch OR variants and exhibiting the same inclination angle with respect to the surface grow preferentially. This affects the compound layer morphology and thickness.

4. After nitriding for 48 hours, when α-Fe is depleted in Si due to pronounced precipitation of X, the compound layer advances by conventional planar type of γ', likely under conditions of or close to local α/γ' equilibrium. Partially displacive growth of Fe nitride becomes of minor importance.

5. ε exists in contact with the nitriding atmosphere under process conditions only allowing for the formation of γ' in pure Fe after all investigated nitriding times of up to 48 hours. This reveals that ε can form and is stable at a lower nitriding potential in the Fe–3wt pctSi alloy than in pure Fe. The present results suggest that the ε/γ' phase boundary in the Fe–Si–N phase diagram may be shifted to a lower chemical potential of N due to the presence of Si, as previously hypothesized in Reference 19 based on nitriding of Fe–C–Si alloys. Note the importance of such effect of Si on the Fe–Si–N phase diagram for tailoring nitriding treatments for Si-alloyed steels and cast irons.

6. Future investigations using high-resolution analytical methods must clarify the local distribution and state of Si in the compound layer and at the growth front of the compound layer in nitrided Fe–Si alloys. This will provide deeper insight into the effect of Si on the growth mechanism and on the thermodynamic stabilities ranges of ε and γ'.

CONFLICT OF INTEREST

On behalf of all authors, the corresponding author states that there is no conflict of interest.

FUNDING

OPEN ACCESS

SUPPLEMENTARY INFORMATION

The online version contains supplementary material available at https://doi.org/10.1007/s11661-021-06441-z.

REFERENCES

1. J. R. Davis, ed.: *Cast Irons,* Materials Park, OH, 1996.
2. F.G. Caballero, M.K. Miller, C. Garcia-Mateo, C. Capdevila, and S.S. Babu: *Acta Mater.*, 2008, vol. 56, pp. 188–99.
3. E. Kozeschnik and H.K.D.H. Bhadeshia: *Mater. Sci. Technol.*, 2008, vol. 24, pp. 343–47.
4. H. Berns and W. Theisen: *Eisenwerkstoffe - Stahl und Gusseisen*, Springer, Berlin, 2008.

5. L.C. Casteletti, R.M.M. Riofano, and P.A.P. Nascente: *Mater. Sci. Technol.*, 2004, vol. 20, pp. 1171–78.
6. R.M.M. Riofano, L.C. Casteletti, and P.A.P. Nascente: *J. Mater. Eng. Perform.*, 2005, vol. 14, pp. 75–84.
7. W. Zhao, D. Liu, H. Qin, X. Zhang, H. Zhang, R. Zhang, Z. Ren, C. Ma, A. Amanov, Y-S. Pyun, G.L. Doll, Y. Dong, and C. Ye: *Surf. Coat. Technol.*, 2019, vol. 375, pp. 205–14.
8. M. Hernandez, M.H. Staia, and E.S. Puchi-Cabrera: *Surf. Coat. Technol.*, 2008, vol. 202, pp. 1935–43.
9. S.S. Akhtar, A.F.M. Arif, and B.S. Yilbas: *Int. J. Adv. Manuf. Technol.*, 2010, vol. 47, pp. 687–98.
10. J. Baranowska: *Surf. Coat. Technol.*, 1998, vols. 100–101, pp. 271–75.
11. X. Nie, L. Wang, Z.C. Yao, L. Zhang, and F. Cheng: *Surf. Coat. Technol.*, 2005, vol. 200, pp. 1745–50.
12. G. Nicoletto, A. Tucci, and L. Esposito: *Wear*, 1996, vol. 197, pp. 38–44.
13. A. Buchwalder, N. Klose, and R. Zenker: *Metall. Ital.*, 2020, vol. 112, pp. 28–39.
14. T. Liapina, A. Leineweber, E.J. Mittemeijer, and W. Kockelmann: *Acta Mater.*, 2004, vol. 52, pp. 173–80.
15. H.A. Wriedt, N.A. Gokcen, and R.H. Nafziger: *Bull. Alloy Phase Diagrams*, 1987, vol. 8, pp. 355–77.
16. A. Leineweber, H. Jacobs, F. Hüning, H. Lueken, and W. Kockelmann: *J. Alloys Compd.*, 2001, vol. 316, pp. 21–38.
17. H. Jacobs, D. Rechenbach, and U. Zachwieja: *J. Alloys Compd.*, 1995, vol. 227, pp. 10–17.
18. H.P. van Landeghem, M. Gouné, S. Bordère, F. Danoix, and A. Redjaimia: *Acta Mater.*, 2015, vol. 93, pp. 218–34.
19. S. Kante, P. Kürnsteiner, B. Gault, M. Motylenko, and A. Leineweber: *Acta Mater.*, 2021, vol. 209, p. 116774.
20. M.H. Biglari, C.M. Brakman, M.A.J. Somers, W.G. Sloof, and E.J. Mittemeijer: *Z. Metallkd.*, 1993, vol. 84, pp. 124–31.
21. T. Steiner and E.J. Mittemeijer: *J. Mater. Eng. Perform.*, 2016, vol. 25, pp. 2091–102.
22. H. Selg, E. Bischoff, S.R. Meka, R.E. Schacherl, T. Waldenmaier, and E.J. Mittemeijer: *Metall. Mater. Trans. A*, 2013, vol. 44, pp. 4059–70.
23. S.R. Meka, K.S. Jung, E. Bischoff, and E.J. Mittemeijer: *Philos. Mag.*, 2012, vol. 92, pp. 1435–55.
24. B. Schwarz, S.R. Meka, R.E. Schacherl, E. Bischoff, and E.J. Mittemeijer: *Acta Mater.*, 2014, vol. 76, pp. 394–403.
25. B. Schwarz, P.J. Rossi, L. Straßberger, F. Jörg, S.R. Meka, E. Bischoff, R.E. Schacherl, and E.J. Mittemeijer: *Philos. Mag.*, 2014, vol. 94, pp. 3098–119.
26. E.J. Mittemeijer, M.H. Biglari, A.J. Böttger, N.M. van der Pers, W.G. Sloof, and F.D. Tichelaar: *Scripta Mater.*, 1999, vol. 41, pp. 625–30.
27. S.R. Meka, E. Bischoff, B. Rheingans, and E.J. Mittemeijer: *Philos. Mag. Lett.*, 2013, vol. 93, pp. 238–45.
28. H.P. van Landeghem, M. Gouné, T. Epicier, and A. Redjaimia: *Scripta Mater.*, 2013, vol. 68, pp. 187–90.
29. G.R. Booker and J. Norbury: *Nature*, 1959, vol. 184, pp. 1311–12.
30. F. Meng, G. Miyamoto, and T. Furuhara: *Mater. Trans.*, 2021, vol. 62, pp. 596–602.
31. A.M. Maliska, A.N. Klein, and A.R. de Souza: *Surf. Coat. Technol.*, 1995, vol. 70, pp. 175–79.
32. H.P. van Landeghem, M. Gouné, and A. Redjaimia: *Steel Res. Int.*, 2012, vol. 83, pp. 590–93.
33. S.R. Meka and E.J. Mittemeijer: *JOM*, 2013, vol. 65, pp. 769–75.
34. S.R. Meka, A. Schubert, E. Bischoff, and E.J. Mittemeijer: *Metall. Mater. Trans. A*, 2020, vol. 51, pp. 3154–66.
35. Thermo-Calc Software AB: *TCFE Steels/Fe-Alloys Database Version 7*, 2020.
36. H. Atmani and O. Thoumire: *Bull. Mater. Sci.*, 2002, vol. 25, pp. 219–25.
37. V.A. Fedchun and N.V. Silina: *Met. Sci. Heat Treat.*, 1988, vol. 30, pp. 890–95.
38. A. V.C. Sobral, A. C. Boblitz Parente, J. L.R. Muzart, and C. V. Franco: *Surf. Coat. Technol.*, 1997, vol. 92, pp. 10–15.
39. W. Pitsch: *Philos. Mag.*, 1959, vol. 4, pp. 577–84.
40. U. Dahmen, P. Ferguson, and K.H. Westmacott: *Acta Metall.*, 1987, vol. 35, pp. 1037–46.
41. W. Pitsch: *Arch. Eisenhüttenwes.*, 1961, vol. 32, pp. 573–79.
42. H. Schumann, G. Richter, and A. Leineweber: *J. Appl. Crystallogr.*, 2020, vol. 53, pp. 865–79.
43. H. Schumann and A. Leineweber: *Materialia*, 2021, vol. 17, p. 101119.
44. G. Wassermann: *Mitt. Kaiser-Wilhelm-Inst. Eisenforsch.*, 1935, vol. 17, pp. 149–55.
45. Z. Nishiyama: *Sci. Rep. Tohoku Univ.*, 1934, vol. 23, pp. 637–64.
46. W.G. Burgers: *Physica*, 1934, vol. 1, pp. 561–86.
47. D. Gerardin, H. Michel, and M. Gantois: *Scripta Metall.*, 1977, vol. 11, pp. 557–61.
48. D. Gerardin, J.P. Morniroli, H. Michel, and M. Gantois: *J. Mater. Sci.*, 1981, vol. 16, pp. 159–69.
49. E. J. Mittemeijer: *Steel Heat Treating Fundamentals and Processes*, Ed. by J. L. Dossett and G. E. Totten, ASM international, 2013, pp. 619–46.
50. A. Leineweber, T. Gressmann, and E.J. Mittemeijer: *Surf. Coat. Technol.*, 2012, vol. 206, pp. 2780–91.
51. H. Göhring, O. Fabrichnaya, A. Leineweber, and E.J. Mittemeijer: *Metall. Mater. Trans. A*, 2016, vol. 47, pp. 6173–86.
52. A. A. Coelho: *Topas 5*, Bruker AXS GmbH, Karlsruhe.
53. S.I. Wright, M.M. Nowell, S.P. Lindeman, P.P. Camus, M. de Graef, and M.A. Jackson: *Ultramicroscopy*, 2015, vol. 159, pp. 81–94.
54. F. Bachmann, R. Hielscher, and H. Schaeben: *Ultramicroscopy*, 2011, vol. 111, pp. 1720–33.
55. R. Krakow, R. J. Bennett, D. N. Johnstone, Z. Vukmanovic, W. Solano-Alvarez, S. J. Lainé, J. F. Einsle, P. A. Midgley, C. M. F. Rae, and R. Hielscher: *Proc. R. Soc. London, Ser. A*, 2017, vol. 473.
56. G. Nolze and R. Hielscher: *J. Appl. Crystallogr.*, 2016, vol. 49, pp. 1786–1802.
57. S. Kante and A. Leineweber: *Acta Mater.*, 2019, vol. 170, pp. 240–52.
58. A.A. Kodentsov, M.J.H. van Dal, J.K. Kivilahti, and F.J.J. van Loo: *Ber. Bunsenges. Phys. Chem.*, 1998, vol. 102, pp. 1326–33.
59. A.A. Kodentsov, M.J.H. van Dal, C. Cserháti, L. Daróczi, and F.J.J. van Loo: *Acta Mater.*, 1999, vol. 47, pp. 3169–80.
60. A. Holst, A. Buchwalder, and R. Zenker: *Metall. Ital.*, 2020, vol. 112, pp. 61–72.
61. H-J. Spies, H. Biermann, and A. Fischer: *Z. Metallkd.*, 2005, vol. 96, pp. 781–86.
62. J. Martin, A. Martinavicius, S. Bruyère, H.P. van Landeghem, C. Gendarme, F. Danoix, R. Danoix, A. Redjaimia, T. Grosdidier, and T. Czerwiec: *J. Alloys Compd.*, 2016, vol. 683, pp. 418–26.
63. N.M. Le, C. Schimpf, H. Biermann, and A. Dalke: *Metall. Mater. Trans. B*, 2021, vol. 52, pp. 414–24.
64. H. Göhring, A. Leineweber, and E.J. Mittemeijer: *Metall. Mater. Trans. A*, 2016, vol. 47, pp. 4411–24.
65. S.T. Pisarik and D.C. van Aken: *Metall. Mater. Trans. A*, 2014, vol. 45, pp. 3173–78.
66. H.K.D.H. Bhadeshia: *Mater. Sci. Technol.*, 2018, vol. 142, pp. 1–3.
67. S.S. Babu, K. Hono, and T. Sakurai: *Appl. Surf. Sci.*, 1993, vol. 67, pp. 321–27.
68. M. Wohlschlögel, U. Welzel, and E.J. Mittemeijer: *Appl. Phys. Lett.*, 2007, vol. 91, pp. 147–51.
69. M.H. Wetzel, M.R. Schwarz, and A. Leineweber: *J. Alloys Compd.*, 2019, vol. 801, pp. 438–48.